Tuning the optical and photoluminescence properties of high efficient Eu^{3+}-doped KY_3F_{10} phosphors by different synthetic approaches

Pablo Serna-Gallén[1], Héctor Beltrán-Mir[1 *], Eloísa Cordoncillo[1 **]

[1]*Departamento de Química Inorgánica y Orgánica, Universitat Jaume I, Av. Sos Baynat s/n 12071, Castelló de la Plana, Spain*

* mir@uji.es, **cordonci@uji.es

Abstract

Eu^{3+}-doped KY_3F_{10} materials with a dopant content between 0 and 5 mol% were prepared based on the nominal composition $K(Y_{3-x}Eu_x)F_{10}$ using different synthetic routes. The reaction conditions have been proven to be critical factors for the characteristics of the final products: morphology, size and crystallinity. As a result, noticeable changes in their photoluminescence spectra and lifetimes were observed. Quantum cutting processes or similar energy transfers between Eu^{3+} ions allowed obtaining high quantum efficiencies, while the analysis of the Ω_2 Judd-Ofelt parameter suggested that the crystal field of Eu^{3+} was very similar in all the compositions. A well-designed synthesis of Ln^{3+}-doped fluorides can provide a full range of opportunities to explore new phenomena. Thus, this study highlights the complexity of the fluoride-based systems, which are exceptional candidates for doping with luminescent lanthanide ions and have very important characteristics for their future application in bioanalytics, biomedics or photonics. Indeed, the color-tunable emissions of the phosphors, which vary from orangish to yellow, could be interesting for their application in white light-emitting diodes through their combination with blue chips.

Keywords: fluorides, europium, optical spectroscopy, luminescence, morphology, structure

Graphical Abstract:

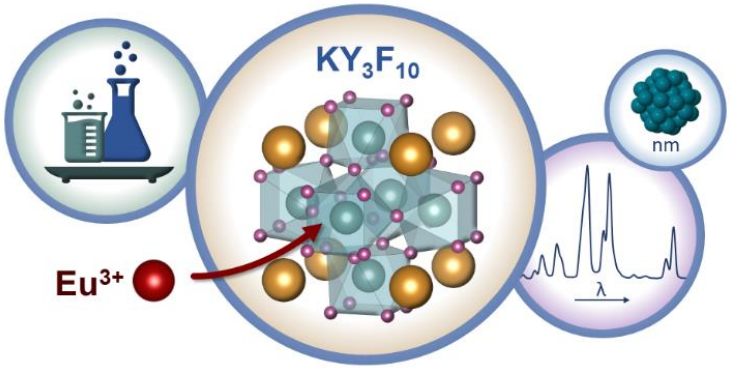

1. Introduction

Over the last few decades, materials doped with luminescent lanthanide ions (Ln^{3+}) have been widely studied because of their application in emitting diodes, solar cells, lasers, and catalysts, among others [1–3]. Fluorides are better host candidates than their respective oxides for optical applications due to the high ionicity of the metal–fluorine bonds, which provides low phonon energy of the crystal lattice (associated with atomic vibrations) [4]. As a result, the quantum efficiencies of the photoluminescent processes are higher and the lifetimes of Ln^{3+} are longer, varying from a few microseconds to several milliseconds [5].

In addition, fluorides have also been used as upconversion (UC) phosphors [6–8]. Indeed, lanthanide-doped phosphors are of great interest for UC because their electronic configuration makes them more suitable for the absorption of a second photon [9]. For instance, upconverting fluorides have been reported to be promising

materials for bioanalytical and biomedical applications, such as bio-imaging [10,11]. Novel multifunctional materials have also been designed combining the luminescence properties of Ln^{3+}-doped fluorides with the plasmonic activity of metallic nanoparticles (NPs) [12–14]. Therefore, spectroscopic techniques based on plasmonic interactions, such as the well-known Surface Enhanced Raman Spectroscopy (SERS), allow us to detect and quantify different analytes with great sensitivity [15].

On the other hand, white light-emitting diodes (w-LEDs) have lately received attention because of their good stability in their physical and chemical properties. One of the most common strategies to generate these devices is the combination of orange-yellow-emitting phosphors (such as the well-known yellow-emitting $Y_3Al_5O_{12}:Ce^{3+}$) with blue InGaN chips [16]. Nevertheless, the main drawback of this combination is the modest color-rendering index. Additionally, it is also possible to combine near-ultraviolet LED chips with tricolor (red, green, blue) phosphors [17]. Thus, it is still important to develop and optimize the luminescence properties of new orangish-yellow-emitting phosphors. For this reason, many studies have used phosphors based on oxides, phosphates or nitrides matrices [18–21], although fluorides have also been proved recently to be good candidates for w-LEDs [22]. Indeed, the high quantum efficiencies and long lifetimes of fluoride-based structures (due to the low phonon interaction of the host lattice) open up new strategies to the design of materials with interesting properties for their applications in such devices.

Fluoride crystals supporting trivalent lattice cations (such as Y^{3+}) are especially attractive for luminescence because they allow their isovalent substitution for a lanthanide ion [23]. The potassium-yttrium-fluorine system has been studied and has

yielded many phases: KYF_4, KY_2F_7, KY_3F_{10}, KY_7F_{22}, K_2YF_5 and K_3YF_6 [24–29]. Of these, KY_3F_{10} has attracted a lot of attention because of its spectroscopic properties over a wide range of temperatures [4,30]. Moreover, KY_3F_{10} crystal melts congruently and is a suitable host for Ln^{3+} ions, which can easily substitute Y^{3+} ions in a non-center-symmetrical site (C_{4v} symmetry) [31,32].

Under ambient conditions, KY_3F_{10} crystallizes in a face-centered cubic structure (fluorite-type structure) belonging to the $Fm\bar{3}m$ (O_h^5) space group, with lattice parameter a = 11.536 Å, cell volume V = 1535.20 Å^3, and 8 formula units per unit cell (Z = 8) [33]. The crystallographic parameters are detailed in Table 1.

Table 1. Distribution of KY_3F_{10} atoms in space group $Fm\bar{3}m$ (no. 225) [33].

Name	Species	Wyckoff Position	Local Symmetry	Atomic Coordinates		
				x	*y*	*z*
K	K^+	8*c*	T_d	1/4	1/4	1/4
Y	Y^{3+}	24*e*	C_{4v}	0.2401	0	0
F1	F^-	32*f*	C_{2v}	0.1081	0.1081	0.1081
F2	F^-	48*i*	C_{3v}	1/2	0.1647	0.1647

The structure can be described as square antiprisms composed of YF_8 units. A central cation of yttrium is linked to two squares of non-equivalent fluorine anions. One square contains four anions in 32*f* sites (F1), while the other is composed of four anions in 48*i* sites (F2) [34], Figure 1(a). The union of six antiprisms generates a cluster-type assemblage, whose edges are shared, leaving an empty cuboctahedron in the center formed by ions in position 48*i*, Figure 1(b). The empty cuboctahedra are situated at the center of the unit cell and in the middle of its edges, Figure 1(c). The potassium cations

are distributed along channels running parallel to the *a*, *b* and *c* crystallographic axes [35]. Structures were drawn with VESTA software [36].

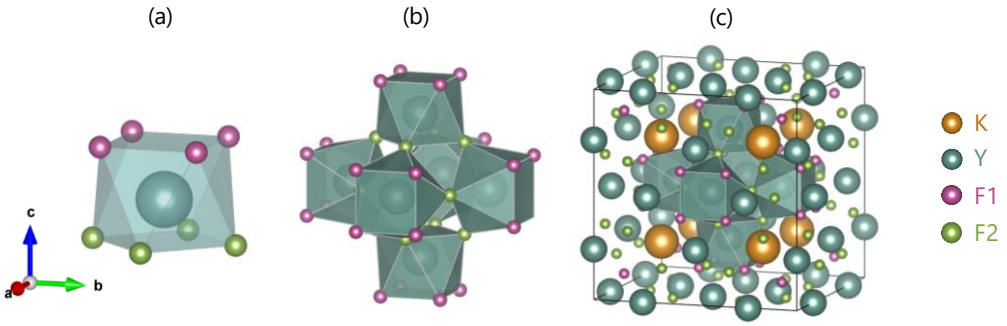

Figure 1. Structure of cubic KY_3F_{10}: (a) basic unit composed of YF_8 square antiprisms, (b) cluster assemblage of six antiprisms, and (c) unit cell.

KY_3F_{10} compounds have been synthesized via different methods, including the hydrothermal method, coprecipitation or sonochemical processes, giving rise to nano/micron-sized materials with different morphologies (spherical, semi-spherical, rodlike, etc.) [12,13,32,37–40]. However, these preparation methods are frequently problematic to use because of the complexity and difficulties involved in the reproducibility of the product [38].

The structural and optical properties of KY_3F_{10} have also been reported in the literature. Nevertheless, to the best of our knowledge, no accurate attempts have been made to provide a full analysis of different synthetic procedures that studies their influence on the luminescence features of these materials. Among all the lanthanides, we have chosen Eu^{3+} as a dopant ion in view of its adequacy as a site-sensitive structural probe [41–43], which can be useful to discuss the optical response of the materials. In addition, the ionic radius for Y^{3+} (coordination number, CN = 8) is 1.019 Å

and for Eu^{3+} (CN = 8), it is 1.066 Å [44]. Therefore, these similar values ensure a good incorporation of the Eu^{3+} ions in KY_3F_{10}.

The luminescence properties of the materials are highly dependent on their size, shape, and structure. A well-designed and controlled synthesis of Ln^{3+}-doped fluorides can provide a full range of opportunities to explore new phenomena [45,46]. In view of this, the present paper is focused on the study of the structural, morphological, and luminescence properties of Eu^{3+}-doped KY_3F_{10} materials. This study enriches the literature and also reveals the effects of post-hydrothermal treatments on the as-synthesized materials. In addition, we show that quantum cutting processes or similar energy transfers between Eu^{3+} ions allow yielding quantum efficiencies higher than 100%. For all of this, the materials investigated (with highly tunable properties) offer different possibilities depending on the synthesis process used, which can be a keystone for future optical, bioanalytical or biomedical applications. Indeed, the color-tunable emissions of the phosphors could be very interesting for their applications in w-LEDs through their combination with blue chips.

2. Experimental section

2.1. Materials

Reagents used were yttrium(III) nitrate hexahydrate [$Y(NO_3)_3{\cdot}6H_2O$ 99.9%, Alfa Aesar], europium(III) nitrate hexahydrate [$Eu(NO_3)_3{\cdot}6H_2O$ 99.9%, Strem Chemicals], potassium hydroxide [KOH 85%, Labkerm], and potassium tetrafluoroborate [KBF_4 96%, Sigma-Aldrich].

2.2. Synthesis of Eu^{3+}-doped KY_3F_{10} compounds

Different synthetic routes were addressed to prepare KY_3F_{10}. On the one hand, the synthesis of KY_3F_{10} was studied by means of the following methods: sonochemical, coprecipitation, and a continuous stirring process. On the other hand, these methods were also combined with a successive hydrothermal treatment in both acidic and basic medium conditions. Calculations were performed to obtain 0.25 g of the final product, giving yields higher than 90%. In all cases, the final volume of the aqueous solution was adjusted to 50 mL. For the sonochemical processes, a *Bandelin Sonorex* ultrasonic bath with a frequency of 35 kHz was used. For the hydrothermal treatments, the temperature was set to 180 ºC for 24 h, and the Teflon-lined vessel used had a total volume of 125 mL.

Samples of KY_3F_{10} with a content of 0, 1, 3 and 5 mol% Eu^{3+} were synthesized according to the nominal formula $K(Y_{3-x}Eu_x)F_{10}$, where x = 0, 0.01, 0.03 and 0.05, respectively. The molar ratio of reagents was $1Ln(NO_3)_3$: $2KBF_4$ (Ln = Eu, Y); this ratio has been previously reported to be efficient for the synthesis of KY_3F_{10} compounds with good homogeneity [39].

The undoped KY_3F_{10} sample (x = 0) was first prepared following the experimental procedures detailed below. In view of the structural and morphological characterization (see the following section) some synthetic routes were repeated incorporating Eu^{3+} into the crystal structure, which allowed us to study the optical properties of the materials. Table 2 summarizes the different synthetic routes evaluated and the abbreviation used for the samples.

Table 2. Nomenclature of the different routes and the compounds synthesized in each one, where *n* indicates the molar percentage of Eu^{3+} in the sample.

Synthetic route	Reference
1) Ultrasonication	*n*%-R1
2) Ultrasonication + Basic Hydrothermal	*n*%-R2
3) Ultrasonication + Acidic Hydrothermal	*n*%-R3
4) Stirring	*n*%-R4
5) Stirring + Basic Hydrothermal	*n*%-R5
6) Stirring + Acidic Hydrothermal	*n*%-R6
7) Coprecipitation	*n*%-R7
8) Coprecipitation + Basic Hydrothermal	*n*%-R8

2.2.1. Synthetic Routes with an Ultrasonication Common Step (Routes 1–3)

The general scheme of the experimental procedure is depicted in Figure 2. In Route 1 (*Ultrasonication*), $Ln(NO_3)_3{\cdot}6H_2O$ (Ln = Eu, Y) was dissolved in water with the appropriate amount of KBF_4, with a resulting pH of 4. Next, this solution was introduced into an ultrasonic bath at room temperature for 24 h, which led to the formation of a white precipitate and a decrease in the pH to 1. The precipitate was then centrifuged, rinsed several times with water, and dried under an infrared lamp.

With the aim of studying the effect of a hydrothermal treatment over the as-obtained precipitate, two more routes were addressed. In Route 2 (*Ultrasonication + Basic Hydrothermal*), the pH of the dispersion obtained after the ultrasonication process was readjusted to 12 by adding KOH 2M. The whole system was transferred into a Teflon-lined vessel and treated hydrothermally for 24 h in a thermally heated autoclave

at 180 ºC. After that, the precipitate was centrifuged, rinsed, and dried. Alternatively, in Route 3 (*Ultrasonication + Acidic Hydrothermal*), the pH of the dispersion obtained after the ultrasonication process was increased to 4 with KOH 2M. The as-formed precipitate was then treated hydrothermally, centrifuged, rinsed, and dried.

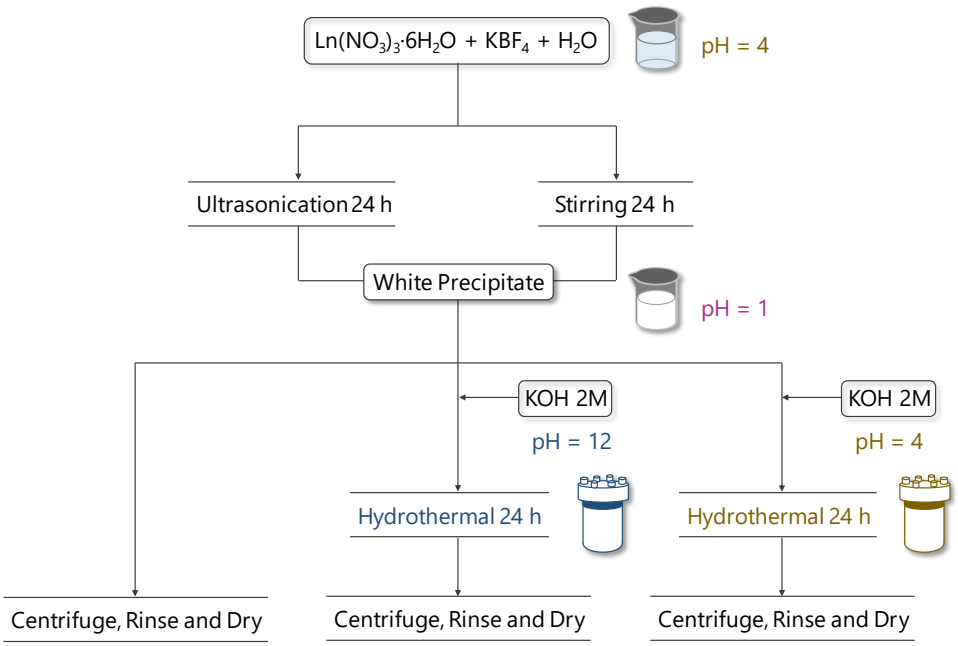

Figure 2. General scheme for the synthetic routes with an ultrasonication common step (Routes 1–3) and with a continuous stirring common step (Routes 4–6).

2.2.2. Synthetic Routes with a Continuous Stirring Common Step (Routes 4–6)

The experimental procedure is the same as for Routes 1–3 (see Figure 2), but with the proviso that instead of ultrasonicating the solution of the reagents, continuous stirring is maintained for 24 h at room temperature. After this time, the presence of a white precipitate was also observed.

2.2.3. Synthetic Routes with a Coprecipitation Common Step (Routes 7–8)

Figure 3 shows the general scheme for the synthesis of the materials following Routes 7–8, with a coprecipitation common step. In Route 7 (*Coprecipitation*), after dissolving the reagents, KOH 2M was added dropwise until a pH of 12 was reached. While doing this, the solution became whitish, indicating the formation of a precipitate. Moreover, in Route 8 (*Coprecipitation* + *Basic Hydrothermal*), the as-formed precipitate was treated hydrothermally for 24 h as previously described for the other routes. Finally, the precipitates were centrifuged, rinsed, and dried.

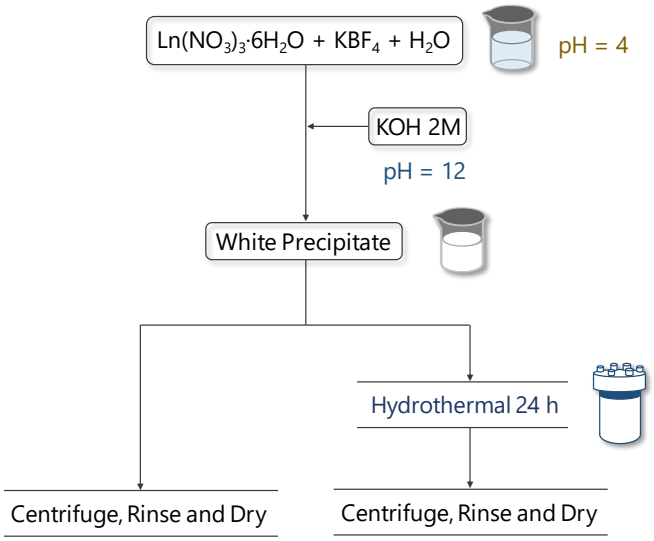

Figure 3. General scheme for the synthetic routes with a coprecipitation common step (Routes 7–8).

2.3. Characterization

All the characterization was carried out at room temperature. Powder X-ray diffraction (XRD) was performed using a Bruker-AX D8-Advance X-ray diffractometer with Cu$K_{\alpha 1}$ radiation at a scan speed of 0.36°/min. All data were collected between 20 ≤ ° 2θ ≤ 90.

Unit cell parameters were refined using WinX^{POW} 1.06 software version. The microstructure of samples was observed using a JEOL 7001F scanning electron microscope (SEM). The operation parameters were: acceleration voltage 15 kV, measuring time 20 s, and working distance 10 mm.

Different optical properties were studied for Eu^{3+}-doped KY_3F_{10} samples with an Eclipse Fluorescence Spectrophotometer (Varian). Excitation spectra were recorded in the range 250–550 nm with an emission wavelength of 593 nm. Emission spectra were performed upon excitation at 395 nm in the range 500–750 nm and normalized to the magnetic dipole $^5D_0 \rightarrow {}^7F_1$ transition. From the spectra, the asymmetry ratio *R* and the Ω_2 Judd-Ofelt parameter were calculated. In addition, the CIE coordinates of the corresponding materials doped with Eu^{3+} were calculated from the emission spectra using the GoCIE software. Time-resolved luminescence measurements were also performed at different emission wavelengths, with the excitation wavelength set to 395 nm. Lifetime values were extracted from decay profiles.

Furthermore, IR spectra were recorded using an Agilent Cary 630 FTIR spectrometer in transmission mode and Raman measurements were performed with a Jasco NRS-3100 Raman spectrometer. The excitation source for the Raman measurements was a 633 nm diode laser with a power of 80 mW at the sample.

3. Results and discussion

3.1. Structural characterization

Figure 4 shows the XRD patterns of the undoped KY_3F_{10} (0% Eu^{3+}) obtained by the different synthetic routes. Figure 4(a) corresponds to the samples of routes with an

ultrasonication common step (Routes 1–3). The XRD patterns show all the peaks corresponding to the cubic phase of KY_3F_{10} (JCPDS-ICDD card 409643). Samples 0%-R1 and 0%-R2 have broad, low-intensity peaks, meaning that the materials may not be so much crystalline or are nano-sized. However, the peaks of sample 0%-R3 are very well defined and, therefore, a higher crystallinity is expected. It is therefore clearly demonstrated that the acidity of the medium in the hydrothermal treatment after the ultrasonication process plays an important role in the final properties of the material. The reactions that take place to form this crystalline phase considering the reagents used are:

$$BF_4^- + 3H_2O \leftrightarrow 3HF + F^- + H_3BO_3 \quad (1)$$

$$K^+ + 3Y^{3+} + 10F^- \rightarrow KY_3F_{10} \quad (2)$$

In view of that, it might be possible that some redissolution processes occurred during the high conditions of pressure in the hydrothermal treatment of the as-formed KY_3F_{10}. In the acidic treatment, the system may evolve through partial redissolution-nucleation-growth processes to particles of larger size, which would explain the narrow peaks found in the XRD pattern of sample 0%-R3. However, with the basic treatment, the as-formed KY_3F_{10} would be stabilized and no changes are found in sample 0%-R2 with respect to 0%-R1. Further work to investigate these possibilities is in progress.

Regarding the XRD results for the routes with a continuous stirring common step (Figure 4(b), Routes 4–6), noticeable changes seem to take place. The diffractogram of the sample 0%-R4 (without hydrothermal treatment) presents the main reflections of cubic KY_3F_{10} together with other more intense peaks associated with a secondary phase

(red stars in Figure 4(b)). However, when the as-obtained precipitate is thermally heated in the autoclave (Routes 5 and 6), the secondary phase disappears and we achieve the stabilization of the crystalline KY_3F_{10} phase. In addition, it is also worth noting that in these routes, the acidic or basic conditions of the medium in the hydrothermal treatment do not have so much influence over the crystallinity, since the diffraction patterns are quite similar. As per the above behavior, we consider that the secondary phase plays an important role when the as-formed precipitate is hydrothermally treated. Possibly, for the thermodynamics of the system in the presence of the secondary phase, the redissolution-nucleation-growth processes are not affected by the pH level in the hydrothermal treatment, which allows the formation of crystalline KY_3F_{10} with very similar characteristics regardless of the medium acidity.

With regard to Figure 4(c), we must emphasize the absence of any diffraction peak in sample 0%-R7, thereby indicating that the solid obtained following Route 7 is mainly amorphous. Despite this, when this solid is treated under hydrothermal conditions (Route 8), the crystalline phase of cubic KY_3F_{10} is formed. It is important to note that coprecipitation synthesis often results in amorphous products as a first phase, generally composed of hydroxide-type compounds. During the hydrothermal treatment, the reactivity of the as-formed precipitate is highly enhanced due to the high pressure achieved in the system. As a result, the amorphous precipitates can undergo several phase transformations which lead them to a crystalline structure.

As a conclusion, the XRD results reveal that the hydrothermal treatments and the acidity of the medium can have a great impact on the crystallinity of the samples depending on the synthetic route. Additionally, the unit cell parameters of the undoped

samples having single phase were refined. The results were in good agreement with the reported values for cubic KY_3F_{10}, although no remarkable differences can be found between samples of different synthetic routes (see Supporting Information, Table S1).

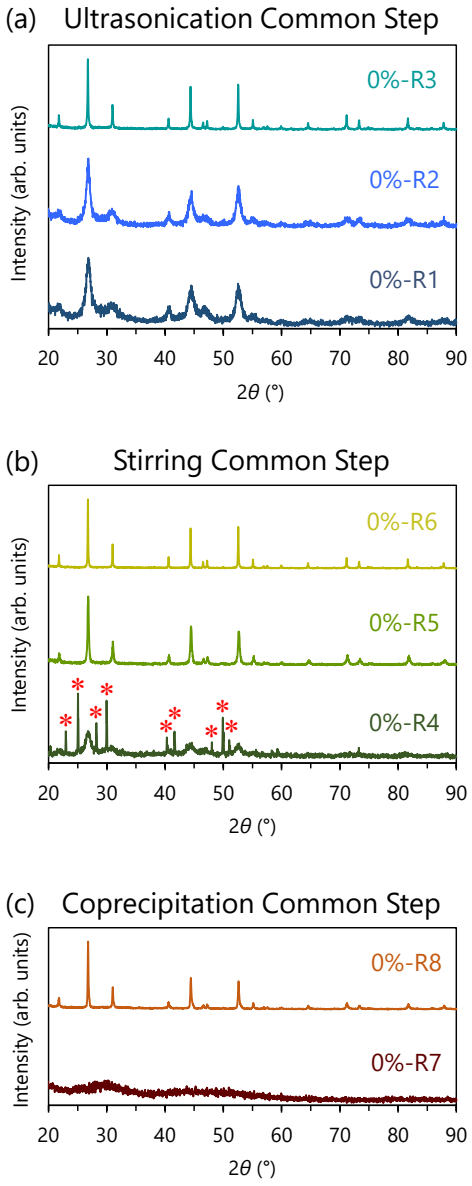

Figure 4. XRD patterns for the different 0% Eu^{3+} samples of the synthetic routes with a common step of (a) ultrasonication, Routes 1–3; (b) continuous stirring, Routes 4–6; and (c) coprecipitation, Routes 7–8. Red stars in (b) highlight the presence of a secondary phase.

3.2. Morphological characterization

Figure 5 shows the SEM images of the undoped KY_3F_{10} (0% Eu^{3+}) obtained by the different synthetic procedures. Figure 5(a-c) corresponds to the samples of routes with an ultrasonication common step (Routes 1–3). The morphologies observed are in good agreement with the XRD results, since the samples with the same XRD profile (0%-R1 and 0%-R2) also have a very similar microstructure, Figure 5(a-b). These materials are formed by spherical particles with a diameter range from 100 to 400 nm. In addition, they are self-assembled from nanoparticles with a diameter of about 10 nm, which would explain the XRD broad peaks. These results are also in agreement with the ones obtained by L. Zhu *et al*. [39] following a similar synthesis to obtain KY_3F_{10} compounds. Regarding the 0%-R3 sample, Figure 5(c), there is a clear evolution of the spherical morphology. There are particles of about 400 nm (whose geometry is less defined) around which nanoparticles of 50 nm have been distributed. This morphological change is attributed to the acidic hydrothermal treatment after the ultrasonication process, as was commented in the previous section.

The morphologies of samples with a continuous stirring common process (Routes 4–6) were also studied by SEM, Figure 5(d-f). Sample 0%-R4, Figure 5(d), is composed of particles of two completely different shapes (octahedrons and spheres). Most of the octahedral particles have sizes closer to 1 μm and could be associated with the highly crystalline secondary phase observed by XRD. In contrast, when the subsequent hydrothermal treatment is carried out, both Routes 5 and 6 lead to the same particle morphology, with no presence of octahedral shapes, Figure 5(e-f). The greater particles might be formed from the respective octahedrons during the hydrothermal conditions. Moreover, this microstructure is very similar to that of sample 0%-R3.

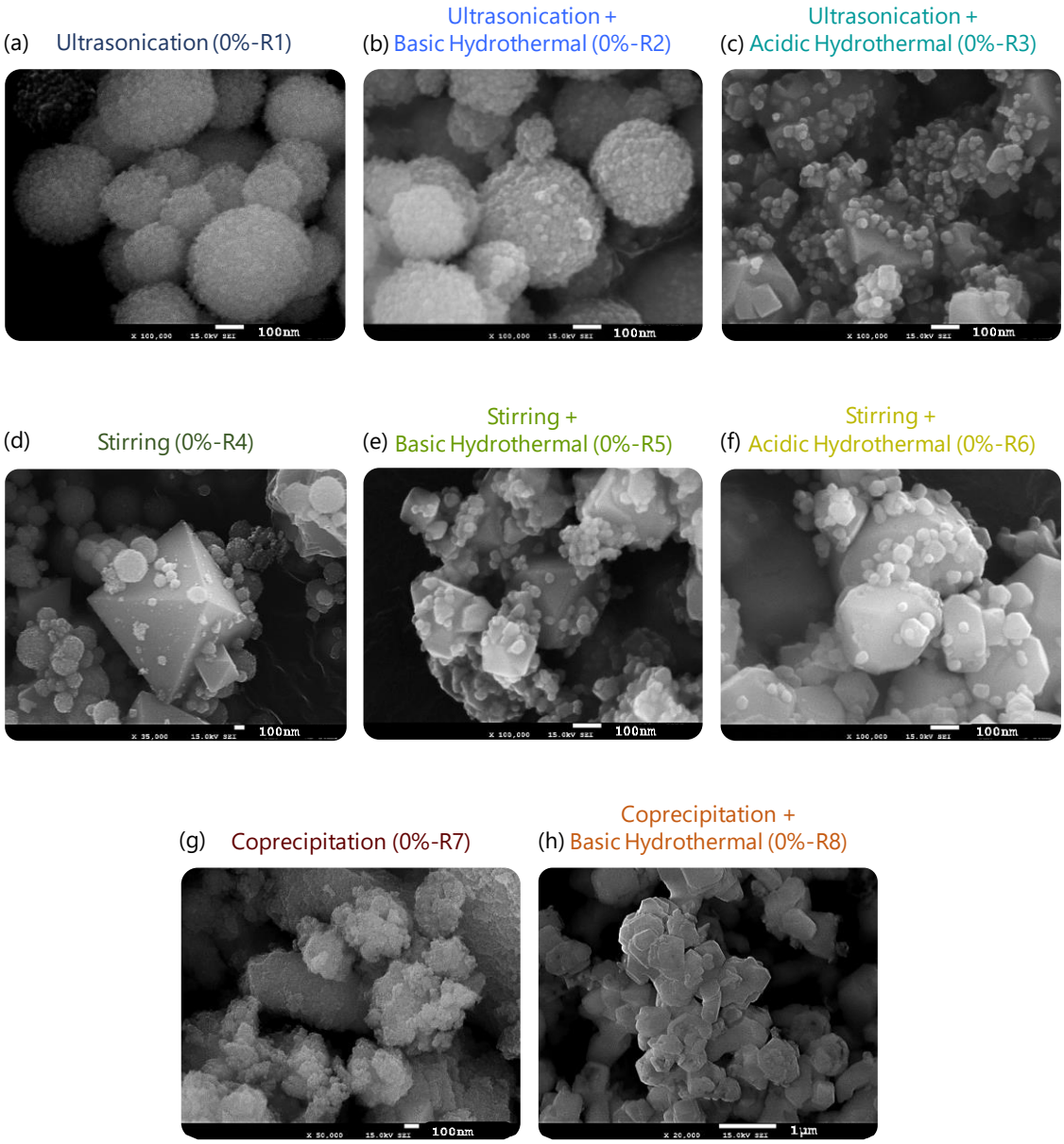

Figure 5. SEM images for the different 0% Eu^{3+} samples of the synthetic routes with a common step of (a-c) ultrasonication, Routes 1–3; (d-f) continuous stirring, Routes 4–6; and (g-h) coprecipitation, Routes 7–8.

Finally, the amorphous character of sample 0%-R7 is also evident with its heterogeneous morphology, Figure 5(g). There are particle aggregates for which neither the geometry nor the size is defined. However, when this precipitate is subsequently treated hydrothermally (Route 8), the microstructure evolves toward a

system composed of particles that are far more crystalline and defined, although some microstructural disorder still exists, Figure 5(h).

Taking everything into consideration, SEM micrographs of the undoped KY_3F_{10} materials reveal that samples of Routes 1 and 2 have similar morphologies, as well as samples of Routes 3, 5 and 6. In contrast, Route 4 yields a solid with the presence of a secondary phase and, following Route 7, we obtain an amorphous material. Therefore, three synthetic routes were strategically chosen with the aim of studying the possible influence of different morphologies over the luminescent response of Eu^{3+}. To carry out the study of the optical properties, samples of KY_3F_{10} with a content of 1, 3 and 5 mol% Eu^{3+} were synthesized following the experimental procedure of Routes 1, 3 and 8. The other synthetic routes were disregarded for similitude in the morphology of the materials, the presence of secondary phases, or the absence of crystallinity. It must be noted that Eu^{3+}-doped KY_3F_{10} materials presented the same XRD patterns and morphologies as their respective undoped compounds.

3.3. Photoluminescence studies

3.3.1. Emission spectra

All the excitation spectra were very similar (see Supporting Information, Figure S1). Neither the Eu^{3+} concentration nor the experimental route seemed to have much influence. This result implies that probably the environment around Eu^{3+} in the crystal host lattice is very similar, as will be discussed later with the Judd-Ofelt and Asymmetry Ratio parameters. Different bands associated with the Eu^{3+} transitions were observed from the ground level $^7F_0$ to the different excited levels. Among all of them, the most

intense was the $^7F_0 \rightarrow {}^5L_6$ transition, with a maximum at 395 nm. Therefore, emission spectra were recorded using this value as the excitation wavelength and were normalized to the magnetic dipole $^5D_0 \rightarrow {}^7F_1$ transition.

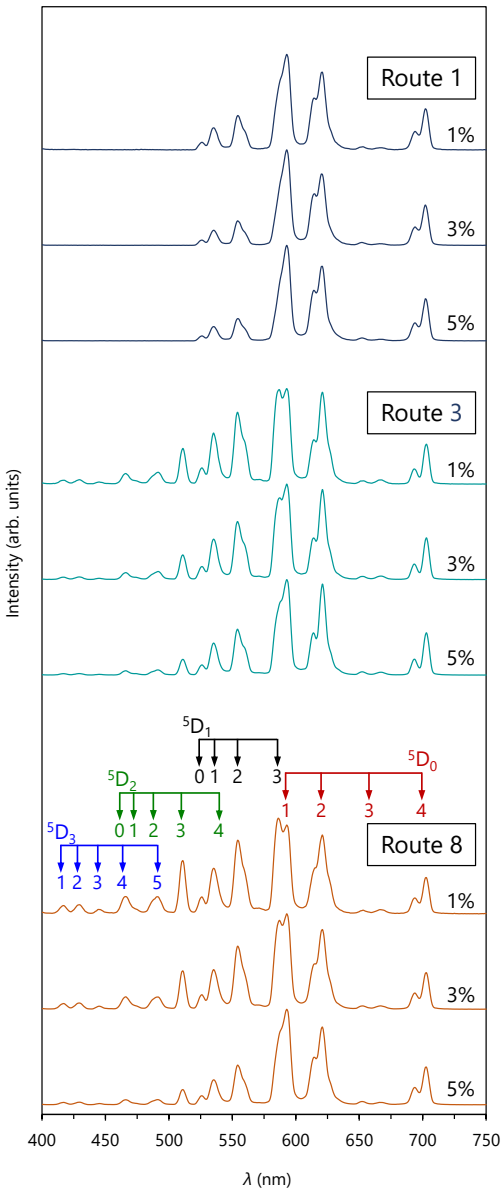

Figure 6. Room temperature emission spectra obtained with a delay time of 0.2 ms upon excitation at 395 nm for samples of Routes 1, 3 and 8 with different molar percentage of Eu^{3+} (1, 3 and 5%). The numbers down the rows indicate the value of *J* associated with the respective transition $^5D_i \rightarrow {}^7F_J$.

Figure 6 shows the emission spectra corresponding to the samples of Routes 1, 3 and 8 with different Eu^{3+} concentrations (1, 3 and 5%) obtained with a delay time (DT)

of 0.2 ms. The spectra show a complex behavior due the mixing of some $^5D_{1\text{-}3} \rightarrow {}^7F_J$ transitions. The emission bands are assigned to the following transitions [47]: $^5D_3 \rightarrow {}^7F_1$ (417 nm), $^5D_3 \rightarrow {}^7F_2$ (429 nm), $^5D_3 \rightarrow {}^7F_3$ (445 nm), $^5D_2 \rightarrow {}^7F_3$ (511 nm), $^5D_1 \rightarrow {}^7F_0$ (526 nm), $^5D_1 \rightarrow {}^7F_2$ (554 nm), $^5D_1 \rightarrow {}^7F_3$ (586 nm), $^5D_0 \rightarrow {}^7F_1$ (593 nm), $^5D_0 \rightarrow {}^7F_2$ (600–635 nm, with the most intense peak at 621 nm), $^5D_0 \rightarrow {}^7F_3$ (650–670 nm) and $^5D_0 \rightarrow {}^7F_4$ (690–710 nm). Those emission bands arising from possible mixing of different transitions (see Figure 6) have not been considered to avoid misleading interpretations. Luminescence measurements of samples 0%-R1, 0%-R3 and 0%-R8 were also performed in order to check if there were any optical response to consider apart from the 4*f*-4*f* transitions of Eu^{3+} that appear in the doped samples. However, the undoped samples showed a total absence of optical response.

From the emission spectra in Figure 6 (DT = 0.2 ms), attention must be drawn to the presence of bands associated with transitions occurring from the higher excited levels $^5D_{1\text{-}3}$. For the Eu^{3+} ion, whether the emission can occur from higher excited levels or not depends critically upon the doping concentration of Eu^{3+} and the dominant vibration frequencies available in the host lattice [48]. As it has been commented previously in the introductory section, the phonon energy of fluorides is low, allowing these transitions to occur.

Samples of Routes 3 and 8 present similar spectral profiles. Nevertheless, the samples of Route 1 deserve some specific comments. The most interesting fact is the absence of the $^5D_{2,3} \rightarrow {}^7F_J$ transitions. As a result, it can be expected that the phonon energy associated with the lattice is higher in these samples in comparison to those of Routes 3 and 8, where these transitions exist. This is also consistent with a lower

intensity of the $^5D_1 \rightarrow {}^7F_J$ transitions. In fact, the $^5D_1 \rightarrow {}^7F_3$ transition appears almost totally convoluted with the $^5D_0 \rightarrow {}^7F_1$ transition. There is not a splitting of the most intense peak (593 nm) as in the samples prepared by other routes, although the presence of the $^5D_1 \rightarrow {}^7F_3$ transition can be inferred in the band from the shoulder at its high-energy side (compare sample 1%-R1 with 5%-R3 and 5%-R8). As the dopant concentration increases, the shoulder tends to disappear as well. A reasonable explanation may be found if we consider the particle size of the samples. The spherical particles, Figure 5(a,b), are self-assembled from nanoparticles with a diameter of about 10 nm. Therefore, due to possible quantum confinement effects, the Ln^{3+} ions may be closer in the host lattice, resulting in higher phonon energy and making the system relaxation from $^5D_3$, $^5D_2$ and $^5D_1$ levels to the $^5D_0$ more likely, quenching the $^5D_{2,3} \rightarrow {}^7F_J$ transitions.

Another aspect to highlight is that the intensity of $^5D_{1\text{-}3} \rightarrow {}^7F_J$ transitions decreases as the Eu^{3+} concentration becomes higher. Therefore, the emission from higher excited levels is partially quenched by cross-relaxation occurring between two neighboring Eu^{3+} ions in the lattice. In this non-radiative process, the higher energy emission is quenched in favor of the lower energy level emission according to [49].

Special attention might be paid to the relative intensity of the $^5D_0 \rightarrow {}^7F_1$ transition (the magnetic dipole one) and $^5D_1 \rightarrow {}^7F_3$. Apart from the absence of the splitting for samples of Route 1 (explained above), with the increase in the dopant concentration, the peak corresponding to the $^5D_0 \rightarrow {}^7F_1$ transition becomes more intense at the expense of the $^5D_1 \rightarrow {}^7F_3$, thus implying that the cross-relaxation process is taking place. This behavior agrees well with the established assignation for the two-component band. If the peak at 586 nm had not corresponded to the $^5D_1 \rightarrow {}^7F_3$ transition, no noticeable decrease in

its intensity would probably have been observed when increasing the cross-relaxation process.

Referring to the previous emission bands assignation, at first glance some misunderstanding may occur regarding the two-component bands that appear between 575–600 and 600–635 nm. Indeed, the peak at 586 nm could either fit the $^5D_1 \rightarrow {}^7F_3$ transition or be part of the $^5D_0 \rightarrow {}^7F_1$. A similar question may also arise for the peak at 621 nm, which could either fit the $^5D_1 \rightarrow {}^7F_4$ transition or be part of the $^5D_0 \rightarrow {}^7F_2$. Further experiments were carried out in order to confirm the previous assignations, as outlined in the following.

The Eu^{3+} lifetimes associated with the transitions occurring from the $^5D_{1,2,3}$ higher energy levels are expected to be lower than the lifetimes associated with transitions from the $^5D_0$ ground level. If the detector delay time (DT) is changed, we can observe the evolution of these transitions and ensure that the assignation of some of the previous two-component bands is accurate. Figure 7 displays the emission spectra of sample 1%-R8 recorded at different delay times. As the DT increases, the intensity of $^5D_{1\text{-}3} \rightarrow {}^7F_J$ transitions diminishes gradually, and only the transitions from the $^5D_0$ ground level at a DT of 10 ms are observable. The peak at 586 nm disappears at 10 ms, indicating that it corresponds to the $^5D_1 \rightarrow {}^7F_3$ transition rather than being a component of the $^5D_0 \rightarrow {}^7F_1$. However, the two peaks at 616 and 621 nm remain at 10 ms, proving that both of them are associated with the $^5D_0 \rightarrow {}^7F_2$ transition. In addition, at this DT the long tail of the $^5D_0 \rightarrow {}^7F_2$ transition becomes narrower and the splitting of the band is also more prominent. This result could be associated with the presence of an additional component as a result of a small contribution from the $^5D_1 \rightarrow {}^7F_4$ transition at a DT of

0.2 ms. The $^5D_0 \rightarrow {}^7F_0$ transition was not observed, although it could have been overlapped with the $^5D_0 \rightarrow {}^7F_1$ band due to its typical low intensity. Similar behavior was observed for samples 1%-R1 and 1%-R3 (see Supporting Information, Figure S2).

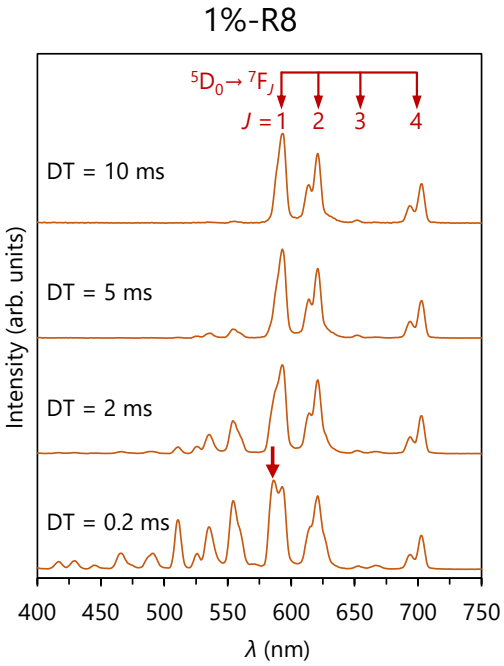

Figure 7. Room temperature emission spectra obtained at different delay times for sample 1%-R8 upon excitation at 395 nm.

The evaluation of the cut-off phonon energy (the highest-energy vibrational mode) for KY_3F_{10} has been ambiguous in the literature, with values obtained in the range 400–600 cm^{-1} [23,50,51]. In order to have a deeper knowledge of the phonon energy and get a general idea on how the lattice vibrations may vary depending on the morphology of samples, IR and Raman spectroscopy was performed for the undoped KY_3F_{10} samples of Routes 1, 3 and 8, as presented in Figure 8.

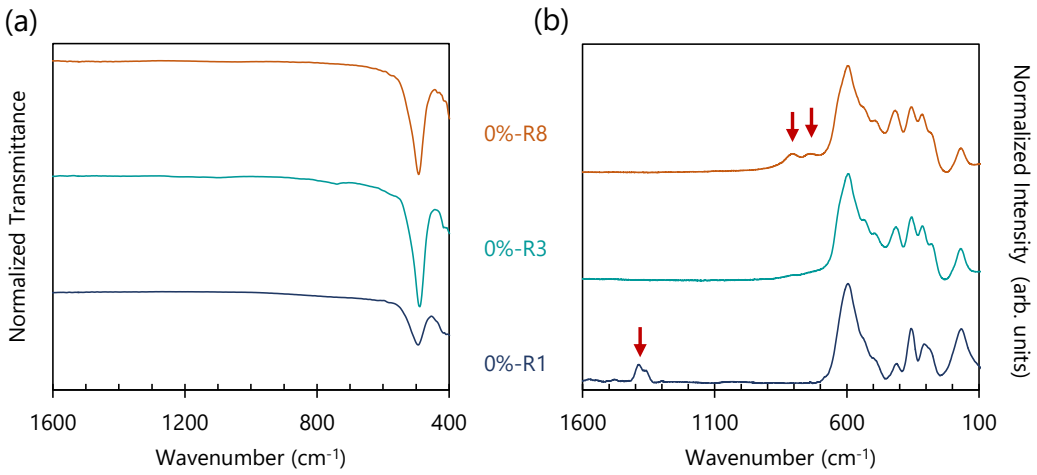

Figure 8. Room temperature (a) IR, and (b) Raman spectra for the undoped KY_3F_{10} samples of Routes 1, 3 and 8.

Regarding the IR spectra, there are no differences among all the samples, which present a unique band centered at 492 cm^{-1}. In the low-frequency region of the Raman spectra (below 700 cm^{-1}), all samples display the same bands with very similar positions and relative intensities, the main dominant peak occurring at 592 cm^{-1}. However, substantial changes appear at higher frequencies depending on the sample. Therefore, the compounds exhibit different cut-off phonon energies, which can be directly related to the photoluminescence behavior of the materials. The sample of Route 8 presents two additional peaks at 731 and 810 cm^{-1}, but the higher cut-off energy is observed for the sample of Route 1, whose Raman spectrum displays two peaks at 1361 and 1391 cm^{-1}. These results are in total agreement with the previous discussion of the changes observed in the transitions occurring from higher excited levels. The differences between samples may arise from the particle size and morphology. Particularly, from the analysis of the Raman spectra it is clear that the sample synthesized following Route 1 has the highest phonon energy. Probably, the small size of the particles (self-assembled nanoparticles with a diameter of about 10 nm)

enhances the presence of quantum confinement effects making that the Ln^{3+} ions are closer in the host lattice and, thus, increasing the cut-off energy of it. A thorough description of the assignation of Raman bands can be found in Section S4 of Supporting Information.

Furthermore, the bar chart in Figure 9(a) presents the values of the total integrated luminescence intensity for the different Eu^{3+}-doped phosphors. It can be seen that the emission intensity depends strongly on both the synthetic route and the dopant concentration. The lowest values correspond to samples of Route 1. Following with the previous line of reasoning, a higher phonon interaction with the luminescent ions could be the critical factor responsible for the intensity quenching. On the other hand, when increasing the dopant content from 3 to 5 mol%, minor changes are appreciated in the emission intensity of samples from Routes 3 and 8.

In addition, the CIE coordinates of the corresponding materials doped with Eu^{3+} were calculated from the emission spectra using the GoCIE software [52] and are shown in Figure 9(b). It is worthy of praise emphasizing that the choice of the synthetic route and dopant content allowed strategically to obtain color-tunable emissions of the phosphors, which vary from orangish to yellow colors and are, therefore, potential candidates for their application in solid state lighting devices, such as blue-InGaN chips based w-LEDs.

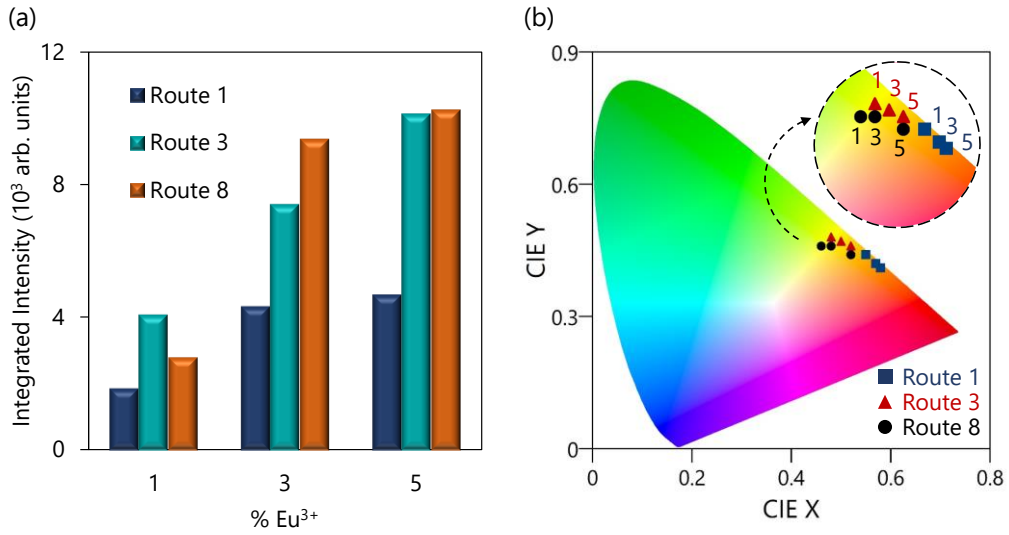

Figure 9. (a) Integrated luminescence intensity and (b) CIE chromaticity diagram for Eu^{3+}-doped samples of Routes 1, 3 and 8 excited by 395 nm. The numbers in the inset indicate the molar percentage of Eu^{3+} (1, 3 and 5%).

3.3.2. Judd-Ofelt and Asymmetry Ratio Calculations

The Judd-Ofelt theory describes the transition intensities for lanthanides and actinides in solids and solutions. According to this theory, the central ion is affected by the surrounding host ions, which produce a static electric field (the crystal field) [53]. The Ω_2 Judd-Ofelt parameter correlates with the polarizable and covalent character of the lanthanide ion in the lattice [54,55]. Thus, the analysis of this parameter can be useful to describe the Eu^{3+} surroundings in the host lattice. Moreover, the intensity of the magnetic dipole $^5D_0 \rightarrow {}^7F_1$ transition is considered to be independent of the host matrix, while the electric dipole $^5D_0 \rightarrow {}^7F_2$ is known as a hypersensitive transition because it is highly influenced by the local symmetry of the Eu^{3+} ion [56]. Therefore, the asymmetry ratio *R* provides information about the local symmetry of the dopant and is defined as the ratio between the intensities of the $^5D_0 \rightarrow {}^7F_2$ and $^5D_0 \rightarrow {}^7F_1$ transitions:

$$R = \frac{I_{02}}{I_{01}} \quad (3)$$

where I_{0J} is the intensity associated with the transition $^5D_0 \rightarrow {}^7F_J$ that takes place at a λ_{0J} wavelength. For Eu^{3+}, the asymmetry ratio is proportional to the Judd-Ofelt parameter Ω_2, which can be calculated from the experimental emission spectra according to the following expression [57]:

$$\Omega_2 = A_{01} \cdot R \cdot \frac{{\lambda_{02}}^4}{\lambda_{01}} \cdot \frac{3h}{64e^2\pi^4\,\chi\,\|U^2\|} \quad (4)$$

where A_{01} is the magnetic dipole transition rate, which is assumed to be constant and equal to 50 s^{-1}; h is the Planck constant; e denotes the elementary charge; χ is the Lorentz local field correction term (which is equal to $\frac{n(n^2+2)^2}{9}$, n is the refractive index at λ_{02}); and $\|U^2\|$ corresponds to the reduced matrix element of the unit tensor operator connecting levels 0–2 [58].

The value reported in the literature for $\|U^2\|$ is 0.0032 [59]. The maximum wavelength value obtained for samples is 593 nm for λ_{01} ($^5D_0 \rightarrow {}^7F_1$ transition) and 621 nm for λ_{02} ($^5D_0 \rightarrow {}^7F_2$ transition). The refractive index of KY_3F_{10} at 621 nm is 1.490 and can be considered as a constant in the spectrum range 470–700 nm [60,61]. Expressing λ_{0J} in cm, taking h = 6.6261·10^{-27} erg·s, e = 4.803·10^{-10} esu, and substituting the rest of the values [62], Ω_2 can be expressed as:

$$\Omega_2 = (1.837\,R) \cdot 10^{-20}\ \text{cm}^2 \quad (5)$$

The calculation of the asymmetry ratio R was performed using the integrated intensities corresponding to the respective emission bands. To avoid the contributions from higher excited levels ($^5D_{1\text{-}3}$), which could lead to non-accurate results, the intensity

values were extracted from the emission spectra recorded with a DT of 10 ms, Figure 7. All the R and Ω_2 values, summarized in Table 3, are very similar regardless of the synthetic route or the europium concentration. In short, there are no noticeable changes in the polarizability environment of the ion, suggesting that the crystal field of Eu^{3+} must be quite similar in all the samples.

Table 3. R and Ω_2 values obtained from the emission spectra with a DT of 10 ms (λ_{exc}= 395 nm).

Eu^{3+}	R			Ω_2 (10^{-20} cm^2)		
mol %	Route 1	Route 3	Route 8	Route 1	Route 3	Route 8
1	1.03	1.05	0.95	1.89(2)	1.93(2)	1.75(1)
3	1.01	1.04	0.96	1.86(2)	1.91(3)	1.76(1)
5	1.06	1.09	1.00	1.95(3)	2.00(3)	1.84(2)

3.3.3. Lifetimes and Quantum Efficiencies Analysis

In addition to the previous experiments, useful information about the photoluminescence properties can also be obtained from the fluorescence kinetics. In order to study the decay curves for the different $^5D_{0\text{-}3}\rightarrow{}^7F_J$ emissions and evaluate the observed lifetime (τ_{obs}) of the different excited levels, time-resolved luminescence measurements were performed with an excitation wavelength of 395 nm. The experiments were carried out setting a DT of 0.2 ms to collect $^5D_{1,2,3}\rightarrow{}^7F_J$ emissions and a DT of 10 ms to collect $^5D_0\rightarrow{}^7F_J$ transitions and avoid the contribution from higher excited levels that could lead to misleading results. Different emission wavelengths were used according to the respective $^5D_{0\text{-}3}\rightarrow{}^7F_J$ transitions. The decay profiles of the $^5D_{0,1}\rightarrow{}^7F_J$ transitions were fitted by the following single exponential function:

$$I(t) = I_0 \exp\left(\frac{-t}{\tau_{\text{obs}}}\right) \quad (6)$$

where I refers to the intensity as a function of time (t). On the other hand, the decay curves of the $^5D_{2,3} \rightarrow {}^7F_J$ transitions were best fitted to a double exponential model:

$$I(t) = I_1 \exp\left(\frac{-t}{\tau_{\text{obs }1}}\right) + I_2 \exp\left(\frac{-t}{\tau_{\text{obs }2}}\right) \quad (7)$$

This fact could be related to some energy transfer or cross-relaxation processes that quench the luminescence from the higher excited states. When the double exponential model was used, an effective lifetime (τ_{eff}) was calculated according to:

$$\tau_{eff} = \frac{I_1(\tau_{\text{obs }1})^2 + I_2(\tau_{\text{obs }2})^2}{I_1(\tau_{\text{obs }1}) + I_2(\tau_{\text{obs }2})} \quad (8)$$

Some examples of the decay profiles can be found in the Supporting Information, Figure S4. In order to evaluate the quantum efficiencies (the intrinsic quantum yields, η) of the phosphors, the radiative lifetimes (τ_{rad}) of Eu^{3+} can be calculated from the emission spectra directly using the following expression [63–65]:

$$\tau_{\text{rad}} = \frac{I_{01}}{n^3 \cdot I_{\text{total}} \cdot (A_{01})_{\text{vac}}} \quad (9)$$

where I_{01} is the integrated intensity associated with the transition $^5D_0 \rightarrow {}^7F_1$; I_{total} is the integrated intensity of all the spectra corresponding to $^5D_0 \rightarrow {}^7F_J$ transitions; n denotes the refractive of the material (which can be considered equal to 1.490); and $(A_{01})_{\text{vac}}$ is the magnetic dipole transition rate in the vacuum (14.65 s^{-1}). The quantum efficiency of the luminescence material can be evaluated considering the calculated radiative lifetimes and the observed lifetimes for the $^5D_0$ level as follows:

$$\eta = \frac{\tau_{\text{obs}}}{\tau_{\text{rad}}} \tag{10}$$

Table 4. Average observed lifetimes for the different excited levels ($^5D_{0\text{-}3}$) of the Eu^{3+}-KY_3F_{10} phosphors, calculated radiative lifetimes and quantum efficiencies for the $^5D_0$ level.

Sample	$\langle\tau_{\text{obs}}\rangle$ (ms)				τ_{rad} (ms)	η (%)
	$^5D_3$	$^5D_2$	$^5D_1$	$^5D_0$		
1%-R1	-	-	1.68(6)	8.02(6)	8.32(4)	96
3%-R1	-	-	1.53(6)	8.09(7)	8.27(4)	98
5%-R1	-	-	1.50(8)	8.15(6)	8.07(3)	101
1%-R3	0.45(2)	0.71(1)	2.06(3)	8.98(2)	8.14(4)	110
3%-R3	0.38(1)	0.66(1)	1.94(1)	8.99(7)	8.00(3)	112
5%-R3	0.29(1)	0.56(1)	1.79(1)	9.16(3)	7.84(3)	117
1%-R8	0.61(2)	0.92(4)	2.05(1)	7.93(7)	8.56(4)	93
3%-R8	0.50(2)	0.85(5)	1.97(5)	8.17(7)	8.55(4)	96
5%-R8	0.43(2)	0.73(4)	1.78(1)	8.78(4)	8.35(4)	105

Table 4 summarizes the average observed lifetimes, $\langle\tau_{\text{obs}}\rangle$, for the different excited levels ($^5D_{0\text{-}3}$) of the Eu^{3+}-KY_3F_{10} phosphors. Different transitions of each level were used for the calculation of the average value (a detailed description can be found in Table S3 of the Supporting Information). All the correlation coefficients of the fits (R^2) were ≥ 0.999 and when the decay profiles were fitted to a double exponential model, the lifetime shown refers to τ_{eff}. The calculated radiative lifetimes and quantum efficiencies for the $^5D_0$ level are also listed in Table 4.

From the analysis of the lifetimes, interesting conclusions can be drawn. Firstly, the discussion of the lifetimes associated with the $^5D_3$, $^5D_2$ and $^5D_1$ emissions will be

addressed. From the experimental data, it is clearly shown that they are shorter than those of the low-energy $^5D_0$ emission, as previously suggested. This is because the Eu^{3+} population in higher excited levels relaxes non-radiatively to the metastable $^5D_0$ level by cross-relaxation processes [48]. In addition, when the Eu^{3+} content is increased, the lifetime value for $^5D_{1-3}$ levels becomes shorter. This fact can be well explained considering the cross-relaxation processes too. Furthermore, there are also differences when comparing samples of different routes. Among all the samples with the same mol% Eu^{3+}, samples of Route 1 present the lowest lifetimes for the $^5D_1$ level. This result is consistent with the previous phonon energy comments (indeed, the emission from $^5D_{2,3}$ levels is totally suppressed). However, while for the $^5D_1$ level there are no differences between samples of Routes 3 and 8, different values are obtained for higher excited levels ($^5D_2$ and $^5D_3$), showing the longer lifetimes samples of Route 8. Considering the cut-off phonon energy results, it was expected the inverse situation. Nonetheless, as described below, the phonon energy mainly affects the $^5D_0$ lifetimes for these samples.

Regarding the $^5D_0$ level, all the lifetimes were determined to be about 8–9 ms, collecting the longest lifetime for the sample 5%-R3. When increasing the dopant content in samples of the same route, the lifetime becomes longer as a general tendency. This is due to the more probable relaxation occurring from the higher excited levels that allow increasing the population of the $^5D_0$ level. As it has been shown before, the Raman spectrum of the sample of Route 8 presented two additional peaks at 731 and 810 cm^{-1}, thus increasing the cut-off phonon energy (in comparison with the sample of Route 3). As a result, it was expected that slightly higher lifetimes would be obtained for samples of Route 3, which is now confirmed. Then, it is easy to notice that

the phonon energy differences in these samples mainly affects the $^5D_0$ lifetimes while those of higher excited levels are very similar.

Finally, the quantum efficiencies calculations deserve some particular comments. The values obtained were in the range of 93–117%. Though high quantum efficiencies were expected due to the low phonon energy of the crystal lattice, the obtained values higher than 100% suggest that other processes may take place. The quantum cutting (QC) process allows obtaining luminescent materials with more than 100% efficiency, which can be very interesting for their application in light-emitting diodes. Theoretically, the QC for a single Ln^{3+} is possible. However, competing emissions in the infrared and ultraviolet could prevent efficient visible QC on a single ion [66]. As an alternative, many studies have reported the use of Ln^{3+} ions pairs (Gd^{3+}-Eu^{3+}, Yb^{3+}-Tb^{3+}, Yb^{3+}-Pr^{3+}…) which lead to quantum efficiencies up to 200%. Nevertheless, a few studies have focused on the possibility of obtaining materials with efficient QC processes using only a single luminescent ion. The studies developed by X. Chen *et al.* showed that QC was observable using only Er^{3+} ions, or in the host matrix $YNbO_4$ using Tm^{3+} as activator ions [67,68].

To the best of our knowledge, no efficient QC processes have been addressed for the Eu^{3+} ion as a single luminescent center. However, the study developed by Y. Liu *et al.* [69] demonstrated that QC processes can efficiently occur in $Ba_9Lu_2Si_6O_{24}$:Tb^{3+} via cross-relaxation energy transfers between Tb^{3+} ions. They also observed that the lifetimes speeded up by increasing the Tb^{3+} concentration because the cross-relaxation effects were strengthened. Relating these findings with our results, a plausible explanation for the high quantum efficiencies yielded is that QC or similar energy

transfers may also occur via cross-relaxation energy processes in our materials. Further work to investigate this possibility is in progress.

4. Conclusions

The structure, morphologies and luminescence properties of Eu^{3+}-doped KY_3F_{10} materials have been investigated in detail. The compounds with the nominal formula $K(Y_{3-x}Eu_x)F_{10}$ were prepared according to different synthetic routes. The synthesis was performed via the sonochemical, coprecipitation and continuous stirring methods. Moreover, a combination of these methods with a successive hydrothermal treatment was also addressed. The results obtained allow us to draw the following conclusions:

- The synthetic methodology and the reaction conditions are critical factors for the characteristics of the final products. The synthetic routes provide solids with very different types of morphology, size, and crystallinity.

- The Eu^{3+}-doped KY_3F_{10} samples show the characteristic emission lines corresponding to the $^5D_{0\text{-}3}\rightarrow{}^7F_J$ transitions. The various morphologies and sizes lead to differences in the phonon energy associated with the lattice vibrations, implying noticeable changes in the luminescence spectra. In particular, a total quenching of the $^5D_{2,3}\rightarrow{}^7F_J$ transitions was observed for the samples obtained by an ultrasonication process (with a higher cut-off energy than the others). As a result, color-tunable emissions were obtained, which varied from orangish to yellow colors.

- The calculations of the asymmetry ratio *R* and the Ω_2 Judd-Ofelt parameter report very similar values regardless of the synthetic route or the europium concentration. Bearing in mind the adequacy of the dopant ion as a structural probe, these results suggest that the crystal field of Eu^{3+} must be quite similar.

- Different lifetime values are obtained for the samples depending on the synthetic route and a plausible relation with the cut-off phonon energy of the compounds can be established. Moreover, quantum cutting processes or similar energy transfers between Eu^{3+} ions allow yielding quantum efficiencies higher than 100%.

For the reasons commented above, this study enriches the literature and shows that the investigated Eu^{3+}-doped KY_3F_{10} phosphors offer different possibilities depending on the synthetic strategy used, which can be a keystone for future optical, bioanalytical or biomedical applications. In fact, the orange-yellow emissions of the phosphors could be interesting for their application in w-LEDs through their combination with blue chips.

Acknowledgments

P.S-G, H.B-M, and E.C. thank the Universitat Jaume I (Project UJI-B2019-41) and Ministerio de Economía y Competitividad (Project MAT2016-80410-P) for financial support. P. S.-G. also thanks the Spanish Ministerio de Ciencia, Innovación y Universidades for an FPU predoctoral contract.

References

[1] J. Wu, J. Wang, J. Lin, Y. Xiao, G. Yue, M. Huang, Z. Lan, Y. Huang, L. Fan, S. Yin, T. Sato, Dual functions of YF_3:Eu^{3+} for improving photovoltaic performance of dye-sensitized solar cells, Sci. Rep. 3 (2013) 1–5. https://doi.org/10.1038/srep02058.

[2] B.M. Tissue, Synthesis and Luminescence of Lanthanide Ions in Nanoscale Insulating Hosts, Chem. Mater. 10 (1998) 2837–2845. https://doi.org/10.1021/cm9802245.

[3] T. Grzyb, M. Węcławiak, T. Pędziński, S. Lis, Synthesis, spectroscopic and structural studies on YOF, LaOF and GdOF nanocrystals doped with Eu^{3+}, synthesized via stearic acid method, Opt. Mater. (Amst). 35 (2013) 2226–2233. https://doi.org/10.1016/j.optmat.2013.06.007.

[4] C. Sassoye, G. Patriarche, M. Mortier, High yield syntheses of reactive fluoride $K_{1-x}(Y,Ln)_xF_{1+2x}$ nanoparticles, Opt. Mater. (Amst). 31 (2009) 1177–1183. https://doi.org/10.1016/j.optmat.2008.12.013.

[5] F. Auzel, Upconversion and Anti-Stokes Processes with f and d Ions in Solids, Chem. Rev. 104 (2004) 139–173.

[6] L. Tao, W. Xu, Y. Zhu, L. Xu, H. Zhu, Y. Liu, S. Xu, P. Zhou, H. Song, Modulation of upconversion luminescence in Er^{3+}, Yb^{3+}-codoped lanthanide oxyfluoride (YOF, GdOF, LaOF) inverse opals, J. Mater. Chem. C. 2 (2014) 4186–4195. https://doi.org/10.1039/c4tc00024b.

[7] Y. Zhang, X. Li, D. Geng, M. Shang, H. Lian, Z. Cheng, J. Lin, YOF nano/micro-crystals: Morphology controlled hydrothermal synthesis and luminescence

properties, CrystEngComm. 16 (2014) 2196–2204. https://doi.org/10.1039/c3ce42323a.

[8] G. Yi, H. Lu, S. Zhao, Y. Ge, W. Yang, D. Chen, L.H. Guo, Synthesis, characterization, and biological application of size-controlled nanocrystalline $NaYF_4$:Yb,Er infrared-to-visible up-conversion phosphors, Nano Lett. (2004). https://doi.org/10.1021/nl048680h.

[9] K.K. Markose, R. Anjana, A. Antony, M.K. Jayaraj, Synthesis of Yb^{3+}/Er^{3+} co-doped Y_2O_3, YOF and YF_3 UC phosphors and their application in solar cell for sub-bandgap photon harvesting, J. Lumin. 204 (2018) 448–456. https://doi.org/10.1016/j.jlumin.2018.08.005.

[10] M. Deng, Y. Ma, S. Huang, G. Hu, L. Wang, Monodisperse upconversion $NaYF_4$ nanocrystals: Syntheses and bioapplications, Nano Res. 4 (2011) 685–694. https://doi.org/10.1007/s12274-011-0124-y.

[11] A. Podhorodecki, A. Noculak, M. Banski, B. Sojka, A. Zelazo, J. Misiewicz, J. Cichos, M. Karbowiak, B. Zasonska, D. Horak, B. Sikora, D. Elbaum, T. Dumych, R. Bilyy, M. Szewczyk, Lanthanides Fluorides Doped Nanocrystals for Biomedical Applications, 61 (2014) 115–125. https://doi.org/10.1149/06105.0115ecst.

[12] M. Runowski, Color-tunable up-conversion emission of luminescent-plasmonic, core/shell nanomaterials - KY_3F_{10}:Yb^{3+},Tm^{3+}/SiO_2-NH_2/Au, J. Lumin. 186 (2017) 199–204. https://doi.org/10.1016/j.jlumin.2017.02.032.

[13] M. Runowski, S. Goderski, J. Paczesny, M. Ksiezopolska-Gocalska, A. Ekner-Grzyb, T. Grzyb, J.D. Rybka, M. Giersig, S. Lis, Preparation of Biocompatible, Luminescent-

Plasmonic Core/Shell Nanomaterials Based on Lanthanide and Gold Nanoparticles Exhibiting SERS Effects, J. Phys. Chem. C. 120 (2016) 23788–23798. https://doi.org/10.1021/acs.jpcc.6b06644.

[14] M. Runowski, N. Stopikowska, S. Goderski, S. Lis, Luminescent-plasmonic, lanthanide-doped core/shell nanomaterials modified with Au nanorods – up-conversion luminescence tuning and morphology transformation after NIR laser irradiation, J. Alloys Compd. 762 (2018) 621–630. https://doi.org/10.1016/j.jallcom.2018.05.211.

[15] B. Sharma, R.R. Frontiera, A. Henry, E. Ringe, R.P. Van Duyne, SERS: Materials, applications, and the future, Mater. Today. 15 (2012) 16–25. https://doi.org/10.1016/S1369-7021(12)70017-2.

[16] H. Wu, H. Li, L. Jiang, R. Pang, S. Zhang, D. Li, G. Liu, C. Li, J. Feng, H. Zhang, Design of a mixed-anionic-ligand system for a blue-light-excited orange-yellow emission phosphor $Ba_{1.31}Sr_{3.69}(BO_3)_3Cl:Eu^{2+}$, J. Mater. Chem. C. (2020). https://doi.org/10.1039/c9tc06360a.

[17] Y. Zhang, J. Xu, Q. Cui, B. Yang, Eu^{3+}-doped $Bi_4Si_3O_{12}$ red phosphor for solid state lighting: Microwave synthesis, characterization, photoluminescence properties and thermal quenching mechanisms, Sci. Rep. 7 (2017) 1–12. https://doi.org/10.1038/srep42464.

[18] Y. Zhou, W. Zhuang, Y. Hu, R. Liu, Z. Jiang, Y. Liu, Y. Li, Y. Zheng, L. Chen, J. Zhong, A broad-band orange-yellow-emitting $Lu_2Mg_2Al_2Si_2O_{12}:Ce^{3+}$ phosphor for application in warm white light-emitting diodes, RSC Adv. 7 (2017) 46713–46720. https://doi.org/10.1039/c7ra08760h.

[19] T. Wanjun, Z. Fen, Effect of codoping Ce^{3+} on the luminescence properties of $Sr_9Mg_{1.5}(PO_4)_7:Eu^{2+}$ orange–yellow phosphor, J. Am. Ceram. Soc. 102 (2019) 4632–4639. https://doi.org/10.1111/jace.16311.

[20] W. Sun, Y. Jia, R. Pang, H. Li, T. Ma, D. Li, J. Fu, S. Zhang, L. Jiang, C. Li, $Sr_9Mg_{1.5}(PO_4)_7:Eu^{2+}$: A Novel Broadband Orange-Yellow-Emitting Phosphor for Blue Light-Excited Warm White LEDs, ACS Appl. Mater. Interfaces. 7 (2015) 25219–25226. https://doi.org/10.1021/acsami.5b06961.

[21] L. Liu, R.J. Xie, W. Li, N. Hirosaki, Y. Yamamoto, X. Sun, Yellow-emitting $Y_3Si_6N_{11}$: Ce^{3+} phosphors for white light-emitting diodes (LEDs), J. Am. Ceram. Soc. 96 (2013) 1688–1690. https://doi.org/10.1111/jace.12357.

[22] L.Y. Wang, E.H. Song, T.T. Deng, Y.Y. Zhou, Z.F. Liao, W.R. Zhao, B. Zhou, Q.Y. Zhang, Luminescence properties and warm white LED application of a ternary-alkaline fluoride red phosphor $K_2NaAlF_6:Mn^{4+}$, Dalt. Trans. 46 (2017) 9925–9933. https://doi.org/10.1039/c7dt02036h.

[23] E.N. Silva, A.P. Ayala, J.Y. Gesland, R.L. Moreira, Vibrational spectrum and lattice dynamics of KY_3F_{10} single crystals, Vib. Spectrosc. 37 (2005) 21–26. https://doi.org/10.1016/j.vibspec.2004.05.004.

[24] S. Guo, C. Cao, R. Cao, Synthesis and optical properties of Eu^{3+} doped $NaYF_4$ and KYF_4 micro/nanocrystals, J. Nanosci. Nanotechnol. 16 (2016) 3857–3860. https://doi.org/10.1166/jnn.2016.11792.

[25] P. Caro, P. Porcher, Infra-red excitation of visible luminescence in up-converters rare earth materials, J. Lumin. 18–19 (1979) 257–261. https://doi.org/10.1016/0022-2313(79)90116-9.

[26] K. Friese, H. Krüger, V. Kahlenberg, T. Balić-Zunić, H. Emerich, J.Y. Gesland, A. Grzechnik, Study of the temperature dependence of the structure of KY_3F_{10}, J. Phys. Condens. Matter. 18 (2006) 2677–2687. https://doi.org/10.1088/0953-8984/18/9/007.

[27] L. Aigouy, A. Cazé, P. Gredin, M. Mortier, R. Carminati, Mapping and quantifying electric and magnetic dipole luminescence at the nanoscale, Phys. Rev. Lett. 113 (2014) 1–5. https://doi.org/10.1103/PhysRevLett.113.076101.

[28] P.A. Loiko, N.M. Khaidukov, J. Méndez-Ramos, E. V. Vilejshikova, N.A. Skoptsov, K. V. Yumashev, Up- and down-conversion emissions from Er^{3+} doped K_2YF_5 and K_2YbF_5 crystals, J. Lumin. 170 (2016) 1–7. https://doi.org/10.1016/j.jlumin.2015.10.016.

[29] M.A. Gusowski, A. Gagor, M. Trzebiatowska-Gusowska, W. Ryba-Romanowski, Crystal structure and vibrational properties of new luminescent hosts K_3YF_6 and K_3GdF_6, J. Solid State Chem. 179 (2006) 3145–3150. https://doi.org/10.1016/j.jssc.2006.06.005.

[30] A. Bensalah, M. Ito, Y. Guyot, C. Goutaudier, A. Jouini, A. Brenier, H. Sato, T. Fukuda, G. Boulon, Spectroscopic properties and quenching processes of Yb^{3+} in Fluoride single crystals for laser applications, J. Lumin. 122–123 (2007) 444–446. https://doi.org/10.1016/j.jlumin.2006.01.201.

[31] B. Petrovich Sobolev, The Rare Earth Trifluorides. Part 1. The High Temperature Chemistry of the Rare Earth Trifluorides, first ed., Barcelona, Spain, 2000.

[32] L. Gomes, H.M.D.S.M.D. Linhares, R.U. Ichikawa, L.G. Martinez, S.L. Baldochi, Luminescence properties of Yb:Er:KY_3F_{10} nanophosphor and thermal treatment effects, Opt. Mater. (Amst). 54 (2016) 57–66. https://doi.org/10.1016/j.optmat.2016.02.010.

[33] P. Villars, K. Cenzual, eds., KY_3F_{10} Crystal Structure: Datasheet from "PAULING FILE Multinaries Edition – 2012" in SpringerMaterials (https://materials.springer.com/isp/crystallographic/docs/sd_0552093), (n.d.).

[34] A. Grzechnik, J. Nuss, K. Friese, J.-Y. Gesland, M. Jansen, Refinement of the crystal structure of potassium triyttrium decafluoride, KY_3F_{10}, Z. Krist. NCS. 217 (2002) 460. https://doi.org/10.1524/ncrs.2002.217.jg.460.

[35] R.U. Ichikawa, H.M.S.M.D. Linhares, I. Peral, S.L. Baldochi, I.M. Ranieri, X. Turrillas, L.G. Martinez, Insights into the Local Structure of Tb-Doped KY_3F_{10} Nanoparticles from Synchrotron X-ray Diffraction, ACS Omega. 2 (2017) 5128–5136. https://doi.org/10.1021/acsomega.7b00668.

[36] K. Momma, F. Izumi, VESTA 3 for three-dimensional visualization of crystal, volumetric and morphology data, J. Appl. Crystallogr. 44 (2011) 1272–1276. https://doi.org/10.1107/S0021889811038970.

[37] L. Zhu, Y. Liu, X. Fan, D. Yang, X. Cao, Facile synthesis and luminescence properties of uniform and monodisperse KY_3F_{10}:Ln_3(Ln=Eu, Ce, Tb) nanospheres, J. Lumin. 131 (2011) 1380–1385. https://doi.org/10.1016/j.jlumin.2011.03.024.

[38] S. Goderski, M. Runowski, S. Lis, Synthesis of luminescent KY_3F_{10} nanopowder multi-doped with lanthanide ions by a co-precipitation method, J. Rare Earths. 34 (2016) 808–813. https://doi.org/10.1016/S1002-0721(16)60098-4.

[39] L. Zhu, J. Meng, X. Cao, Sonochemical synthesis of monodispersed KY_3F_{10}:Eu^{3+}nanospheres with bimodal size distribution, Mater. Lett. 62 (2008) 3007–3009. https://doi.org/10.1016/j.matlet.2008.01.096.

[40] C. Cao, Hydrothermal synthesis, phase evolution, and optical properties of Eu^{3+}-doped KF-YF_3 system materials, J. Mater. Res. Soc. 27 (2012) 2988–2995. https://doi.org/10.1557/jmr.2012.331.

[41] C. Cascales, R. Balda, V. Jubera, J.P. Chaminade, J. Fernández, Optical spectroscopic study of Eu^{3+} crystal field sites in $Na_3La_9O_3(BO_3)_8$ crystal., Opt. Express. 16 (2008) 2653–2662. https://doi.org/10.1364/OE.16.002653.

[42] C. Cascales, P. Porcher, J. Fernández, A. Oleaga, R. Balda, E. Diéguez, Crystal field studies in Eu^{3+} doped $Bi_{12}SiO_{20}$ and $Bi_{12}SiO_{20}$:V^{5+} single crystals, J. Alloys Compd. 323–324 (2001) 260–266.

[43] C. Cascales, J. Fernández, R. Balda, Investigation of site-selective symmetries of Eu^{3+} ions in KPb_2Cl_5 by using optical spectroscopy, Opt. Express. 13 (2005) 2141–2152. https://doi.org/10.1364/OPEX.13.002141.

[44] R.D. Shannon, Revised Effective Ionic Radii and Systematic Studies of Interatomic Distances in Halides and Chalcogenides, Acta Crystallogr. A32 (1976) 751–767. https://doi.org/10.1107/S0567739476001551.

[45] I.E. Kolesnikov, A. V. Povolotskiy, D. V. Mamonova, E. Lähderanta, A.A. Manshina, M.D. Mikhailov, Photoluminescence properties of Eu^{3+} ions in yttrium oxide nanoparticles: defect vs. normal sites, RSC Adv. 6 (2016) 76533–76541. https://doi.org/10.1039/c6ra16814k.

[46] G.A. Sotiriou, M. Schneider, S.E. Pratsinis, Green, silica-coated monoclinic Y_2O_3:Tb^{3+} nanophosphors: Flame synthesis and characterization, J. Phys. Chem. C. 116 (2012) 4493–4499. https://doi.org/10.1021/jp211722z.

[47] K. Binnemans, Interpretation of europium(III) spectra, Coord. Chem. Rev. 295 (2015) 1–45. https://doi.org/10.1016/j.ccr.2015.02.015.

[48] X. Liu, L. Yan, J. Lin, Tunable Photoluminescence and Cathodoluminescence Properties of Eu^{3+}-Doped $LaInO_3$ Nanocrystalline Phosphors, J. Electrochem. Soc. 156 (2009) 1–6. https://doi.org/10.1149/1.3002378.

[49] T. Yamase, T. Kobayashi, M. Sugeta, H. Naruke, Europium(III) Luminescence and Intramolecular Energy Transfer Studies of Polyoxometalloeuropates, J. Phys. Chem. A. 101 (1997) 5046–5053.

[50] M. Mortier, J.Y. Gesland, M. Rousseau, M.A. Pimenta, L.O. Ladeira, J.C. Machado da Silva, G.A. Barbosa, Raman Scattering Investigations of KY_3F_{10}, J. Raman Spectrosc. 22 (1991) 393–396. https://doi.org/10.1017/CBO9781107415324.004.

[51] I.R. Martín, Y. Guyot, M.F. Joubert, R.Y. Abdulsabirov, S.L. Korableva, V. V. Semashko, Stark level structure and oscillator strengths of Nd^{3+} ion in different fluoride single crystals, J. Alloys Compd. 323–324 (2001) 763–767. https://doi.org/10.1016/S0925-8388(01)01080-5.

[52] K. R. Justin Thomas, GoCIE V2 software (2009), downloaded from http://faculty.iitr.ac.in/~krjt8fcy/index.html

[53] B.M. Walsh, Judd-Ofelt theory: principles and practices, in: B. Di Bartolo, O. Forte (Eds.), Adv. Spectrosc. Lasers Sens., Springer, Dordrecht, 2006: pp. 403–433.

[54] D.K. Patel, B. Vishwanadh, V. Sudarsan, S.K. Kulshreshtha, Difference in the Nature of Eu^{3+} Environment in Eu^{3+}-Doped $BaTiO_3$ and $BaSnO_3$, J. Am. Ceram. Soc. 96 (2013) 3857–3861. https://doi.org/10.1111/jace.12596.

[55] C. de Mello Donegá, S.A. Junior, G.F. de Sá, Synthesis, luminescence and quantum yields of Eu(III) mixed complexes with 4,4,4-trifluoro-1-phenyl-1,3-butanedione and 1,10-phenanthroline-*N*-oxide, J. Alloys Compd. 250 (1997) 422–426. https://doi.org/10.1016/S0925-8388(96)02562-5.

[56] K. Vuković, M. Medić, M. Sekulić, M.D. Dramićanin, Analysis of Eu^{3+} emission from Mg_2TiO_4 nanoparticles by Judd-Ofelt theory, Adv. Condens. Matter Phys. 2015 (2015) 1–7. https://doi.org/10.1155/2015/736517.

[57] P. Serna-Gallén, H. Beltrán-Mir, E. Cordoncillo, A.R. West, R. Balda, J. Fernández, Site-selective symmetries of Eu^{3+}-doped $BaTiO_3$ ceramics: a structural elucidation by optical spectroscopy, J. Mater. Chem C. 7 (2019) 13976–13985. https://doi.org/10.1039/c9tc03987b.

[58] B. Julián, J. Planelles, E. Cordoncillo, P. Escribano, P. Aschehoug, C. Sanchez, B. Viana, F. Pellé, Eu^{3+}-doped CdS nanocrystals in SiO_2 matrices: One-pot sol-gel synthesis and optical characterization, J. Mater. Chem. 16 (2006) 4612–4618. https://doi.org/10.1039/b612519k.

[59] S. Constantin, M.L. Stanciu, Calculation Of The Judd - Ofelt Parameters Of The $ZnAl_2O_4:Eu^{3+}$, Ann. West Univ. Timisoara - Phys. 56 (2012) 127–131. https://doi.org/10.1515/awutp-2015-0020.

[60] P. Porcher, P. Caro, Crystal field parameters for Eu^{3+} in KY_3F_{10}. II. Intensity parameters, J. Chem. Phys. 68 (1978) 4176–4182. https://doi.org/10.1063/1.436279.

[61] J. Zhang, Z. Hao, X. Zhang, Y. Luo, X. Ren, X.J. Wang, J. Zhang, Color tunable phosphorescence in $KY_3F_{10}:Tb^{3+}$ for x-ray or cathode-ray tubes, J. Appl. Phys. 106 (2009) 034915. https://doi.org/10.1063/1.3190511.

[62] Y.H. Elbashar, D.A. Rayan, Judd Ofelt Study of Absorption Spectrum for Neodymium Doped Borate Glass, Int. J. Appl. Chem. 12 (2016) 59–66.

[63] P. Ghosh, A. Patra, Influence of crystal phase and excitation wavelength on luminescence properties of Eu^{3+}-doped sodium yttrium fluoride nanocrystals, J. Phys. Chem. C. 112 (2008) 19283–19292. https://doi.org/10.1021/jp807539r.

[64] X.-N. Tian, G.-C. Jiang, X.-T. Wei, L.-Y. Wu, S. Li, K.-M. Deng, Y.H. Chen, M. Yin, Synthesis and photoluminescent properties of $NaYF_4:Eu^{3+}$ Core and $NaYF_4:Eu^{3+}/NaYF_4$ core/shell nanocrystals, J. Nanosci. Nanotechnol. 14 (2014) 4490–4494. https://doi.org/10.1166/jnn.2014.8053.

[65] M.H.V. Werts, R.T.F. Jukes, J.W. Verhoeven, The emission spectrum and the radiative lifetime of Eu^{3+} in luminescent lanthanide complexes, Phys. Chem. Chem. Phys. 4 (2002) 1542–1548. https://doi.org/10.1039/b107770h.

[66] R.T. Wegh, H. Donker, E. V.D. Van Loef, K.D. Oskam, A. Meijerink, Quantum cutting through downconversion in rare-earth compounds, J. Lumin. 87 (2000) 1017–1019. https://doi.org/10.1016/S0022-2313(99)00514-1.

[67] X. Chen, J. Wu, X. Xu, Y. Zhang, N. Sawanobori, C. Zhang, Q. Pan, G.J. Salamo, Three-photon infrared quantum cutting from single species of rare-earth Er^{3+} ions in $Er_{0.3}Gd_{0.7}VO_4$ crystalline, Opt. Lett. 34 (2009) 887. https://doi.org/10.1364/ol.34.000887.

[68] X. Chen, G.J. Salamo, S. Li, J. Wang, Y. Guo, Y. Gao, L. He, H. Ma, J. Tao, P. Sun, W. Lin, Q. Liu, Two-photon, three-photon, and four-photon excellent near-infrared quantum cutting luminescence of Tm^{3+} ion activator emerged in Tm^{3+}:$YNbO_4$ powder phosphor one material simultaneously, Phys. B Condens. Matter. 479 (2015) 159–164. https://doi.org/10.1016/j.physb.2015.10.009.

[69] Y. Liu, J. Zhang, C. Zhang, J. Jiang, H. Jiang, High Efficiency Green Phosphor $Ba_9Lu_2Si_6O_{24}$:Tb^{3+}: Visible Quantum Cutting via Cross-Relaxation Energy Transfers, J. Phys. Chem. C. 120 (2016) 2362–2370. https://doi.org/10.1021/acs.jpcc.5b11790.